

Possible orthorhombic phase of Ta_2O_5 under high pressures

Yan Gong(龚艳), Hui-Min Tang(唐慧敏), Yong Yang(杨勇), and Yoshiyuki Kawazoe
Citation: Chin. Phys. B, 2025, 34 (**11**): 116104. DOI: 10.1088/1674-1056/ae0925
http://cpb.iphy.ac.cn; http://iopscience.iop.org/cpb

What follows is a list of articles you may be interested in

Physical properties of high-pressure synthesized $Al_{65}Cu_{20}Fe_{15}$ quasicrystal

Yibo Liu(刘一博), Changzeng Fan(范长增), Zhefeng Xu(许哲峰), Ruidong Fu(付瑞东), Feng Ke(柯峰), Lin Wang(王霖), Bin Wen(温斌), Lifeng Zhang(张立峰), Marek Mihalkovič, and Bo Xu(徐波)
Chin. Phys. B, 2025, 34 (**9**): 096103. DOI: 10.1088/1674-1056/add4fb

Pressure-induced amorphization and metallization in orthorhombic SiP

Qiru Zeng(曾琪茹), Youjun Zhang(张友君), Yukai Zhuang(庄毓凯), Linfei Yang(杨林飞), Qiming Wang(王齐明), and Yi Sun(孙熠)
Chin. Phys. B, 2025, 34 (**9**): 096102. DOI: 10.1088/1674-1056/add4f6

First-principles study on structural, electronic, and superconducting properties of Laves-phase alloy $HfZn_2$ under pressure

Xiao Ma(马晓), Tao Wang(王涛), Jianfeng Wen(文剑锋), Zhenwei Zhou(周振玮), and Hongyu Zhu(朱红玉)
Chin. Phys. B, 2025, 34 (**8**): 086108. DOI: 10.1088/1674-1056/ade5a1

Synergistic improvements in mechanical and thermal performance of TiB_2 solid-solution-based composites

Zhuang Li(李壮), Cun You(由存), Zhihui Li(李志慧), Xuepeng Li(李雪鹏), Guiqian Sun(孙贵乾), Xinglin Wang(王星淋), Qi Jia(贾琪), Qiang Tao(陶强), and Pinwen Zhu(朱品文)
Chin. Phys. B, 2025, 34 (**8**): 086105. DOI: 10.1088/1674-1056/add00c

Layer-dependent structural stability and electronic properties of $CrPS_4$ under high pressure

Jian Zhu(朱健), Dengman Feng(冯登满), Liangyu Wang(王亮予), Liang Li(李亮), Fangfei Li(李芳菲), Qiang Zhou(周强), and Yalan Yan(闫雅兰)
Chin. Phys. B, 2025, 34 (**6**): 066102. DOI: 10.1088/1674-1056/adc65f

---

RAPID COMMUNICATION

Possible orthorhombic phase of Ta_2O_5 under high pressures

Yan Gong(龚艳)[1,2], Hui-Min Tang(唐慧敏)[3], Yong Yang(杨勇)[1,2,†], and Yoshiyuki Kawazoe[4,5]

[1] *Key Laboratory of Photovoltaic and Energy Conservation Materials, Institute of Solid State Physics, HFIPS, Chinese Academy of Sciences, Hefei* 230031, *China*

[2] *Science Island Branch of Graduate School, University of Science and Technology of China, Hefei* 230026, *China*

[3] *College of Physics and Technology, Guangxi Normal University, Guilin* 541004, *China*

[4] *New Industry Creation Hatchery Center (NICHe), Tohoku University,* 6-6-4 *Aoba, Aramaki, Aoba-ku, Sendai, Miyagi* 980-8579, *Japan*

[5] *Department of Physics, SRM University-AP, Amaravati* 522240, *Andhra Pradesh, India*

(Received 7 August 2025; revised manuscript received 8 September 2025; accepted manuscript online 19 September 2025)

A potential orthorhombic phase of Ta_2O_5, designated as Y-Ta_2O_5, is predicted under high-pressure conditions using density functional theory (DFT) combined with structural search algorithms. This phase, containing four formula units per unit cell ($Z = 4$), exhibits the highest Ta–O coordination numbers reported to date. Y-Ta_2O_5 is identified as the most energetically stable form of Ta_2O_5 within the pressure range of approximately 70 GPa to at least 200 GPa. Both standard DFT-GGA and higher-accuracy GW calculations indicate that Y-Ta_2O_5 is a wide-bandgap semiconductor with a direct bandgap. Furthermore, nuclear quantum effects (NQEs) introduce nontrivial corrections to external pressure at fixed volumes, underscoring their significance in high-pressure phase stability analyses.

Keywords: Ta_2O_5, high-pressure, orthorhombic phase, first-principles, nuclear quantum effects

PACS: 61.50.Ks, 63.20.dk, 71.20.Nr

DOI: 10.1088/1674-1056/ae0925 **CSTR:** 32038.14.CPB.ae0925

Tantalum pentoxide (Ta_2O_5), a prototypical wide-bandgap semiconductor, is widely used in optoelectronic materials,[1–5] resistive random-access memory (RRAM),[6–9] and catalysis[10–12] owing to its exceptional dielectric properties, high optical transparency, low reflectivity, and its intrinsic capability for electron–hole separations. These attributes render it particularly suitable for high-performance anti-reflection coatings that significantly enhance light absorption and photoelectric conversion efficiency in solar cells.[13,14] Beyond conventional applications, Ta_2O_5 demonstrates remarkable potential as a UV photodetector material with applications in military sensing and related fields.[15–17] Furthermore, tantalum-based materials exhibit unique multifunctionality, combining superior biocompatibility, chemical inertness, antimicrobial properties, and excellent mechanical performance (including high hardness and wear resistance), making them strategically important for biomedical applications.[18–22] Recent breakthroughs in Ta_2O_5/multi-walled carbon nanotube (MWCNT) heterostructures have yielded photodetectors with substantially enhanced photocurrent and fast response speeds (rise and decay times < 80 ms). This exceptional performance highlights their potential for advanced applications in high-speed optical communications, precision optoelectronics, and real-time environmental monitoring.[23]

Systematic experimental and theoretical studies have confirmed that the crystal structure of Ta_2O_5 exhibits significant environmental dependency. Substantial evidence suggests its phase composition is primarily regulated by temperature and pressure conditions, while preparation methods also significantly influence the final structure. Based on growth conditions, Ta_2O_5 crystal phases can be divided into two categories: (a) ambient-pressure phases and (b) high-pressure phases.[24–26]

Recent research has demonstrated substantial progress in understanding ambient-pressure phases, with notable advancements in both crystallographic and electronic structures[27] (detailed in supplementary materials). The main ambient-pressure phases discovered so far include L_{SR} (space group *Pm*, $Z = 11$, containing 22 Ta and 55 O atoms),[28] L_G (*C112/m*, $Z = 19$),[29] T (*Pmm*2, $Z = 12$),[30] δ (*P6/mmm*, $Z = 2$),[31] β_{AL} (*Pccm*, $Z = 2$),[32] β_R ($Z = 2$),[33] λ (*Pbam*, $Z = 2$),[34] γ (*P*1, $Z = 2$),[35] and γ_1 (*P*-1, $Z = 1$).[36]

In comparison, research on the high-pressure phases of Ta_2O_5 has progressed more slowly. Pressure engineering is one of the most effective methods to tune the crystal structures and physical properties of semiconductor materials, as it can induce structural and electronic changes, potentially leading to novel high-pressure phases with superior physical and chemical performance.[37–39] To date, only two high-pressure phases have been reported: B phase (*C2/c*, $Z = 4$) and Z phase (*C*2, $Z = 2$). The B phase and Z phase were successfully synthesized by Zibrov's team under conditions of 8 GPa and 1470 K,

†Corresponding author. E-mail: yyanglab@issp.ac.cn

© 2025 Chinese Physical Society and IOP Publishing Ltd. All rights, including for text and data mining, AI training, and similar technologies, are reserved.

and characterized using x-ray powder diffraction and high-resolution transmission electron microscopy (HRTEM).[40] Theoretical calculations by Pérez-Walton *et al.* confirmed that within the studied pressure range, the B phase exhibits the highest thermodynamic stability.[24] However, whether new phases emerge at higher pressures remains unknown.

On the other hand, the effects due to the quantum motions of atomic nuclei, or nuclear quantum effects (NQEs),[41–56] are generally neglected in previous studies under high-pressure conditions when the dynamics don't involve light elements (such as hydrogen and its isotopes). We shall demonstrate below that NQEs are not negligible under high pressures.

Based on existing theoretical and experimental studies, the B phase ($Z = 4$) is the most stable known high-pressure polymorph, with the largest number of formula units per unit cell. To date, no stable polymorphs with higher Z values have been reported. Simulations of larger unit cells ($Z > 4$) would significantly increase the computational burden of first-principles structure searches. Within the affordable computational resources, choosing $Z = 4$ provides a balance between accuracy and cost. Accordingly, first-principles structural search on the $Z = 4$ Ta_2O_5 crystal structures has been carried out in this study, successfully predicting a possible new high-pressure phase, Y-Ta_2O_5 (space group *Ibam*). Calculations further demonstrate that, under pressures above 62 GPa, the Y phase exhibits superior thermodynamic stability compared to the B phase. Importantly, this study specifically considers the influence of nuclear quantum effects (NQEs) on external pressure, finding that one of the aspects of NQEs, i.e., zero-point energy (ZPE) leads to significant pressure corrections. This indicates that observable NQEs are not limited to the dynamical processes in systems containing light elements.[41–56]

This work systematically investigated the crystal structures of the Ta_2O_5 system using first-principles calculations based on density functional theory (DFT). We performed a global structural search on the Ta_2O_5 crystal structures with four formula units ($Z = 4$) by combining the VASP code[57,58] with the USPEX crystal structure prediction program[59,60] using an evolutionary algorithm (EA), while employing the VASP and CALYPSO code[61–63] with particle swarm optimization (PSO) to double-check the predicted results. This approach demonstrates significant advantages in identifying stable structures at specific stoichiometric ratios and has been widely employed in high-pressure research, providing crucial support for advancements in the field.[64,65] In structural search, all the calculations adopted the PBE-type general gradient approximation (GGA) exchange–correlation functional[66] with a plane-wave cutoff energy of 600 eV and a k-point mesh spacing of $0.06 \times 2\pi$ Å^{-1}. Through this approach, we successfully identified an orthorhombic structure with a space group of *Ibam*. To achieve higher accuracy of electronic structures, we have employed the GW method[67,68] to correct the band gap values and verified the structural dynamical stability through phonon calculations based on density functional perturbation theory (DFPT).[69] The phonon calculations used a $2 \times 2 \times 2$ supercell with convergence criteria of 1×10^{-9} eV for energy and 3×10^{-4} eV/Å for forces. The computational details and additional information regarding the cross-validation between USPEX and CALYPSO results can be found in the supplementary materials.

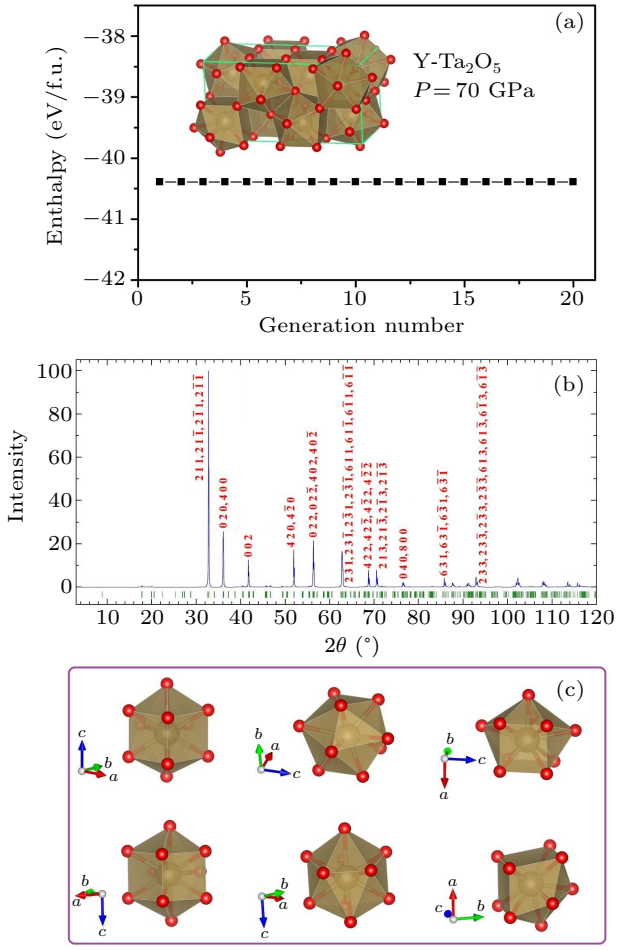


Fig. 1. (a) Enthalpy evolution with generation number for Ta_2O_5 ($Z = 4$) structures at $P = 70$ GPa, calculated using DFT in combination with evolutionary algorithm (EA). (b) Simulated x-ray diffraction pattern using Cu $K\alpha 1$ radiation ($\lambda = 1.541$ Å). (c) Three-dimensional visualization of the fundamental TaO_{10} polyhedral unit (brown spheres: Ta atoms; red spheres: O atoms).

Figure 1(a) presents the results of structural search for Ta_2O_5 at a pressure $P = 70$ GPa, showing excellent energy convergence after 20 generations of evolutionary optimization. The refined Y-phase of Ta_2O_5 crystallizes in the orthorhombic system with an *Ibam* space group, having lattice parameters of $a = 9.939$ Å, $b = 4.977$ Å, $c = 4.322$ Å ($\alpha = \beta = \gamma = 90.00°$). The corresponding atomic coordinates are presented in supplementary materials (Subsection 3.1). Equivalent structures are predicted by VASP + CALYPSO calculations (see supplementary materials, Subsection 3.2 & Table SI). The simulated x-ray diffraction pattern in Fig. 1(b) (Cu $K\alpha 1$ radiation,

$\lambda = 1.541$ Å) displays its strongest peak at $2\theta = 32.81°$ (d-spacing = 2.728 Å) corresponding to (211), (21$\bar{1}$), (2$\bar{1}$1), and (2$\bar{1}\bar{1}$) planes, while the second and third most intense peaks appear at $2\theta = 36.06°$ (d-spacing = 2.488Å, (020) and (400)) and 56.34° (d-spacing = 1.632 Å, (022), (02$\bar{2}$), (402), (40$\bar{2}$)), respectively. As can be seen from Fig. 1(c), compared with the B-phase,[35,36] the Y-phase exhibits higher Ta–O coordination numbers — the highest oxygen coordination number ($n = 10$) known to date in metal oxides. Similar to B-Ta_2O_5, all the building blocks TaO_n of Y-Ta_2O_5 are identical in geometry. Simulations using VASP + USPEX predict that the Y-phase maintains as the most stable structure to at least 200 GPa (see supplementary materials, Subsection 3.3 & Table SII for structural and energy parameters).

Based on enthalpy calculations (see Table 1 and detailed analysis below), we determined that the pressure for the structural transformation from the B-phase to the Y-phase is approximately 62 GPa. At $P = 62$ GPa, although the zero-point energies (ZPE) of both phases are nearly identical (with the Y-phase slightly higher) and the internal energy of equilibrium lattice (E_0) of the B-phase is lower, the Y-phase has a smaller unit cell volume with more compact Ta–O stacking, which accounts for its lower enthalpy value.

To study the dynamical stability and lattice vibration characteristics of Y-Ta_2O_5, we conducted systematic phonon spectrum calculations, based on density functional perturbation theory (DFPT). This approach enables accurate calculation of the system's phonon properties directly at the primitive cell scale, significantly reducing computational costs.[70] Figure 2(a) displays the phonon dispersion curves along high-symmetry directions in the Brillouin zone and the corresponding vibrational density of states (VDOS) of Y-Ta_2O_5. Notably, no imaginary frequencies are observed throughout the Brillouin zone for either acoustic or optical branches, strongly confirming the excellent dynamic stability of the Y-Ta_2O_5 structure.

Table 1. Unit cell and energy parameters describing the Y- and B-Ta_2O_5 at external pressure $P = 62$ GPa. The volume of unit cell (V_{cell}), the zero-point energies (ZPE), and the difference of internal energy and enthalpy with reference to Y-Ta_2O_5 (ΔE_0, ΔH) are listed.

Ta_2O_5	Y	B
a (Å)	9.985	13.596
b (Å)	4.995	4.378
c (Å)	4.347	5.083
α (°)	90.00	90.00
β (°)	90.00	129.22
γ (°)	90.00	90.00
Space group	*Ibam* (No. 72)	$C2/c$ (No. 15)
TaO_n	TaO_{10} (×8)	TaO_8 (×8)
V_{cell} (Å^3/f.u.)	54.20	58.61
ΔE_0 (eV/f.u.)	0	−1.69
ZPE (eV/f.u.)	0.66	0.65
ΔH (eV/f.u.)	0	0.01

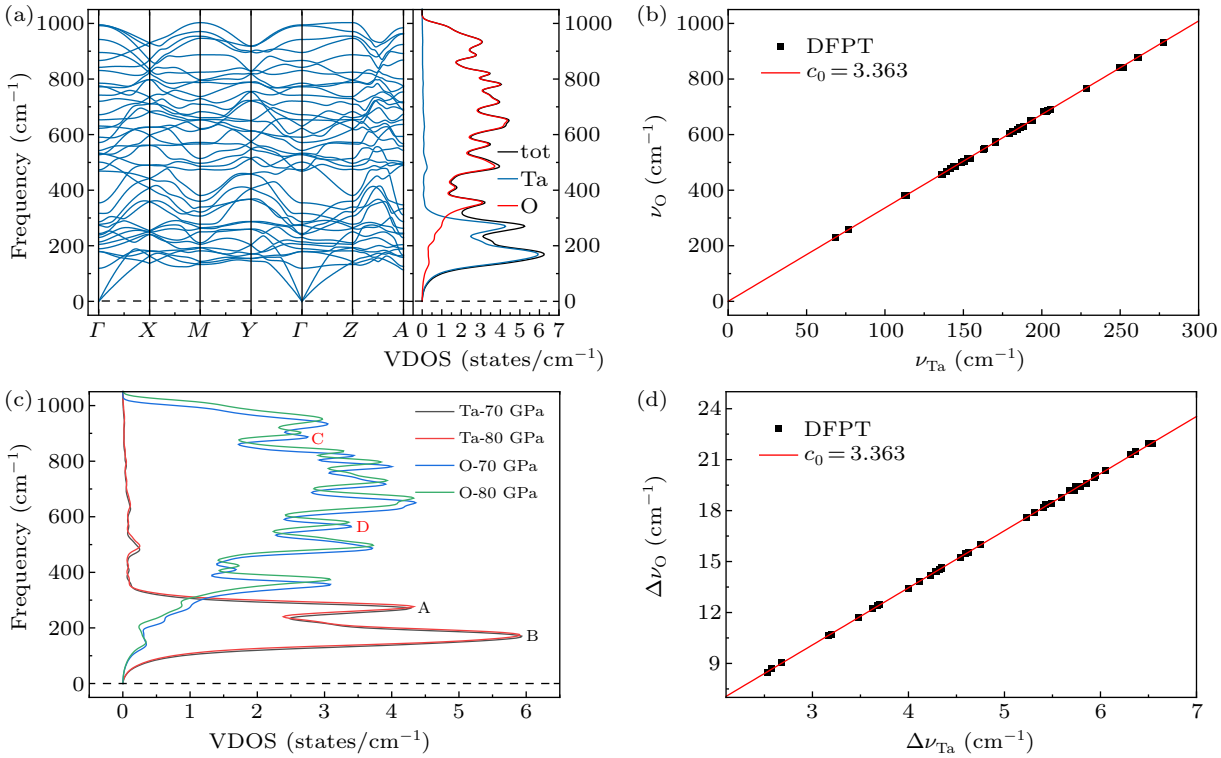


Fig. 2. (a) Calculated phonon dispersion relations (left panel) along high-symmetry q-point paths in the Brillouin zone (BZ) and vibrational density of states (VDOS, right panel) for Y-Ta_2O_5 at 70 GPa. The direct coordinates of q-points in the BZ are defined as $\Gamma = (0,0,0)$, $X = (0.5,0,0)$, $M = (0.5,0.5,0)$, $Y = (0,0.5,0)$, $Z = (0,0,0.5)$, $A = (0.5,0.5,0.5)$. (b) Frequency correspondence of Ta- and O-dominated vibrational modes at 70 GPa. (c) Atom-resolved VDOS and pressure-induced blueshifts at $P = 70$ GPa, 80 GPa. (d) The frequency blueshift correspondence of Ta- and O-dominated vibrational modes under different pressures.

Through atom-projected VDOS analysis [Figs. 2(a) and 2(c)], we observed distinct frequency partitioning in the vibrational modes of Ta and O atoms: the heavier Ta atoms (relative atomic mass 180.95 amu) predominantly contribute to low-frequency vibrational modes ($\nu < 300\ \mathrm{cm}^{-1}$), while the lighter O atoms (relative atomic mass 16.00 amu) dominate the high-frequency region ($\nu > 300\ \mathrm{cm}^{-1}$). This observation can be explained within the model of harmonic oscillator. Generally, for crystals whose primitive cells contain different types of atoms, when the vibrations of one type of atom dominate while the vibrations of other types can be neglected, it can be shown under the harmonic approximation that the vibration frequency ν is inversely proportional to the square root of the atomic mass M:[71] $\nu \propto 1/\sqrt{M}$. For Ta_2O_5, the frequency of each Ta-dominated optical mode and that of the O-dominated optical modes can be correlated one-to-one. Shown in Fig. 2(b) are the frequencies of a number of Ta-dominated optical modes and O-dominated optical modes, where excellent agreement with the prediction of harmonic approximation is found. For example, the two VDOS peaks (A, B) marked in Fig. 2(c), which are mainly due to the vibrations of Ta atoms, find their correspondence of two peaks (C, D) in the high frequency region. Details of the vibrational modes are provided in the supplementary materials (Fig. S1). Furthermore, increased pressure leads to decreased Ta–O distances and therefore stronger interatomic interactions (i.e., force constants) and blueshifts of frequencies, as demonstrated by Fig. 2(c) where the external pressure increases from 70 GPa to 80 GPa. It can be shown that the magnitude of frequency variation ($\Delta\nu$) is also inversely proportional to the square root of the atomic mass M ($\Delta\nu \propto 1/\sqrt{M}$). Based on the mass ratio of Ta (180.95 amu) to O (16.00 amu), the theoretically predicted frequency ratio $c_0 = \nu_O/\nu_{Ta} = (M_O/M_{Ta})^{-1/2} \approx 3.363$, the lines with this slope correspond well with the DFPT frequencies and frequency blueshifts data shown in Figs. 2(b) and 2(d). This explains why heavier Ta atoms tend to exhibit low-frequency vibrations, while lighter O atoms dominate the high-frequency modes.

Figure 3 presents a comprehensive comparison of the electronic structures of Y-Ta_2O_5 and B-Ta_2O_5 under high-pressure conditions. Through combined DFT-GGA (PBE) and GW calculations, we identify distinct electronic behaviors: the Y-phase exhibits a direct bandgap at Γ point (GW: 3.17 eV; PBE: 2.27 eV), contrasting with the B-phase's indirect bandgap characteristic with $\Gamma \to M$ transitions (GW: 3.64 eV; PBE: 2.67 eV). Remarkably, both the valence band maximum (VBM = 9.29 eV) and conduction band minimum (CBM = 12.46 eV) in the Y-phase show significant upward shifts of +2.12 eV and +1.65 eV respectively relative to the B-phase values (VBM = 7.17 eV; CBM = 10.81 eV). These electronic structure modifications originate from pronounced pressure-enhanced orbital hybridization and electron cloud redistribution effects in the Y-phase. While the Y-phase displays a marginally smaller bandgap (by 0.47 eV) compared to the B-phase, its elevated energy level alignment suggests enhanced charge transport capabilities under high pressure. These findings provide crucial insights for the possibility of developing advanced high-pressure electronic devices.

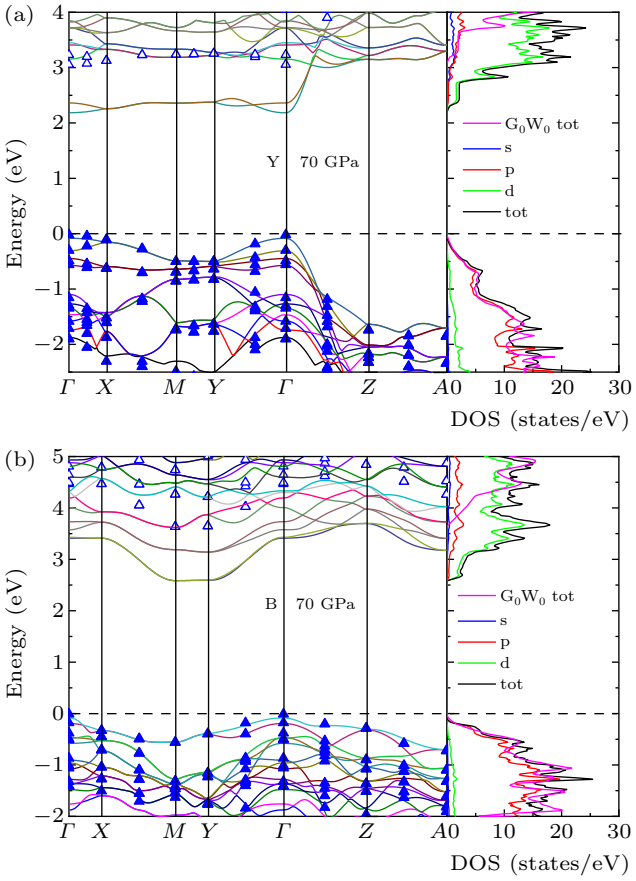


Fig. 3. The electron band structures, density of states (DOS), and partial density of states (PDOS) for Y- (upper panels) and B-Ta_2O_5 (lower panels) at $P = 70$ GPa, calculated using both DFT-GGA and GW methods. In the band structure plot, the solid lines represent the GGA energy bands along high-symmetry k-point paths, while the scattered solid and hollow blue triangles denote the GW results. The Fermi level (indicated by the vertical dashed line) is set at 0 eV.

Table 2. The valence band maximum (VBM), conduction band minimum (CBM) and band gap (E_g) of the two Ta_2O_5 phases (Y, B) at $P = 70$ GPa obtained using DFT-GW method. The DFT-GGA data are listed in parentheses.

Ta_2O_5	VBM (eV)	CBM (eV)	E_g (eV)
Y	9.29 (8.81)	12.46 (11.08)	3.17 (2.27)
B	7.17 (6.78)	10.81 (9.45)	3.64 (2.67)

The quantization of collective vibrations of atoms (more precisely, atomic nuclei) in crystal lattices manifests itself in the form of phonons.[72] The notable blueshifts of vibrational frequencies displayed in Fig. 2 imply the possibility of studying NQEs under high pressures. Generally, the external pressure exerted on a given crystal with volume V at temperature

T may be calculated as follows:[73]

$$\begin{aligned} P &= -\frac{\mathrm{d}U}{\mathrm{d}V} - \frac{\mathrm{d}E_{\mathrm{ph}}}{\mathrm{d}V} \\ &= -\frac{\mathrm{d}U}{\mathrm{d}V} - \sum_j \left(\frac{1}{2}\hbar + \frac{\hbar}{\mathrm{e}^{\hbar\omega_j/(k_{\mathrm{B}}T)}-1}\right)\frac{\mathrm{d}\omega_j}{\mathrm{d}V} \\ &= P_0 + \Delta P, \end{aligned} \tag{1}$$

where U is the internal energy of the equilibrium lattice at volume V, which can be readily obtained using DFT calculations, and $P_0 = -\mathrm{d}U/\mathrm{d}V$ is the pressure without taking into account NQEs; the phonon energy $E_{\mathrm{ph}} = \sum_j (\frac{1}{2}\hbar\omega_j + \frac{\hbar\omega_j}{\mathrm{e}^{\hbar\omega_j/(k_{\mathrm{B}}T)}-1})$, $\hbar$ is the reduced Planck constant and ω_j is the frequency of the jth mode. The correction to pressure due to NQEs is then given by

$$\begin{aligned} \Delta P &= -\frac{\mathrm{d}E_{\mathrm{ph}}}{\mathrm{d}V} = -\sum_j \left(\frac{1}{2}\hbar + \frac{\hbar}{\mathrm{e}^{\hbar\omega_j/(k_{\mathrm{B}}T)}-1}\right)\frac{\mathrm{d}\omega_j}{\mathrm{d}V} \\ &= -\sum_j \left(\frac{1}{2}\hbar\omega_j + \frac{\hbar\omega_j}{\mathrm{e}^{\hbar\omega_j/(k_{\mathrm{B}}T)}-1}\right)\frac{1}{V}\times\frac{\mathrm{d}\ln\omega_j}{\mathrm{d}\ln V}. \end{aligned} \tag{2}$$

At room-temperature and below, the phonon energy is predominantly contributed by ZPE, i.e., $E_{\mathrm{ph}} \cong \sum_j \frac{1}{2}\hbar\omega_j = \mathrm{ZPE}$. Consequently, the correction to pressure due to lattice vibrations can be expressed as follows:

$$\begin{aligned} P &\cong -\frac{\mathrm{d}U}{\mathrm{d}V} - \frac{\mathrm{d}\mathrm{ZPE}}{\mathrm{d}V} = P_0 + \Delta P \\ &= P_0 - \frac{1}{2}\hbar\sum_j \left(\frac{\mathrm{d}\omega_j}{\mathrm{d}V}\right) = P_0 - \sum_j \left(\frac{1}{2}\hbar\omega_j\right)\frac{1}{V}\times\frac{\mathrm{d}\ln\omega_j}{\mathrm{d}\ln V}. \end{aligned} \tag{3}$$

To evaluate the role of NQEs, we proceed to calculate the pressures at target volumes via two numerical schemes. In the first scheme, we calculated the total energy E_{tot} of Y-Ta_2O_5 at different volumes V, and the $E_{\mathrm{tot}} \sim V$ data are least-squares fitted to the third-order Birch–Murnaghan (BM) equation of state (EOS)[74,75] using VASPKIT:[76]

$$\begin{aligned} E_{\mathrm{tot}}(V) &= E_{\mathrm{tot0}} + \frac{9V_0B_0}{16}\left\{\left[\left(\frac{V_0}{V}\right)^{2/3}-1\right]^3 B_0' \right. \\ &\left. + \left[\left(\frac{V_0}{V}\right)^{2/3}-1\right]^2\left[6-4\left(\frac{V_0}{V}\right)^{2/3}\right]\right\}, \end{aligned} \tag{4}$$

where the terms E_{tot0} and V_0 represent the total energy and volume at equilibrium (the external pressure $P = 0$), respectively; and B and B_0' represent the bulk modulus and its pressure derivative at equilibrium volume V_0 at which $E_{\mathrm{tot}}(V)$ reaches its minimum. The role of NQEs is studied when the term E_{tot0} takes into account the ZPE of each volume. The parameters B and B_0' for the third-order BM EOS of the Y phase are listed in supplementary materials (Table SIII). Compared with the first-order Murnaghan EOS,[77] the third-order BM EOS significantly improves fitting accuracy in high-pressure regimes by incorporating nonlinear terms, establishing itself as a widely used formula for studying material behavior under high pressures.[78] The pressure is determined using the third-order BM EOS

$$\begin{aligned} P = -\left(\frac{\partial E_{\mathrm{tot}}}{\partial V}\right) &= \frac{3B_0}{2}\left[\left(\frac{V_0}{V}\right)^{7/3} - \left(\frac{V_0}{V}\right)^{5/3}\right] \\ &\times\left\{1 + \frac{3}{4}\left(B_0'-4\right)\left[\left(\frac{V_0}{V}\right)^{2/3}-1\right]\right\}. \end{aligned} \tag{5}$$

In the second scheme, we utilize the approximation by assuming that for all modes ω_j the term $-\frac{\mathrm{d}\ln\omega_j}{\mathrm{d}\ln V} \cong \gamma$, which is the Grüneisen parameter. Then Eq. (1) can be rewritten as follows:

$$\begin{aligned} P &\cong -\frac{\mathrm{d}U}{\mathrm{d}V} + \frac{\gamma}{V}\sum_j \left(\frac{1}{2}\hbar\omega_j + \frac{\hbar\omega_j}{\mathrm{e}^{\hbar\omega_j/(k_{\mathrm{B}}T)}-1}\right) \\ &= -\frac{\mathrm{d}U}{\mathrm{d}V} + \frac{\gamma}{V}E_{\mathrm{ph}} = P_0 + \Delta P, \end{aligned} \tag{6}$$

where P_0 is readily obtained by DFT calculations, and the second term (ΔP) can be deduced using the Grüneisen parameter and phonon energy. In the room-temperature and cryogenic regimes, $E_{\mathrm{ph}} \cong \mathrm{ZPE}$, and therefore one has $\Delta P \cong (\gamma/V)\mathrm{ZPE}$.

We go further to demonstrate the pressure correction due to NQEs around the critical point of phase transition from B to Y phase. The total energies with and without ZPE corrections versus volume are shown in Fig. 4(a), where good agreement is found for the DFT data and their numerical fitting curves, validating the applicability of third-order BM EOS across this pressure regime. Figure 4(b) plots the dependence of $\ln(\mathrm{ZPE}(V)/\mathrm{ZPE}(V_0))$ with $\ln(V_0/V)$, where a pronounced linear relation is found, and the slope of which yields a Grüneisen parameter of $\gamma \sim 1.78$. An approximately linear drop of ZPE with volume is also found in the vicinity of the phase transition (inset of Fig. 4(b)). The pressures computed using the two schemes (labeled as P_1 and P_2, respectively) to include NQEs are shown in Fig. 4(c), together with the uncorrected data (P_0). The data in Fig. 4(c) reveal remarkable consistency between the two independent approaches for determining ZPE-induced pressure corrections: EOS fitting and Grüneisen approximation, with the correction magnitude remaining essentially constant (~ 3.5 GPa). From Eq. (3), $P \cong -\frac{\mathrm{d}E_0}{\mathrm{d}V} - \frac{\mathrm{d}\mathrm{ZPE}}{\mathrm{d}V} = P_0 + \Delta P$, if the ZPE follows an approximately linear relationship with volume variation — as illustrated in the inset of Fig. 4(b) with $\frac{\mathrm{d}\mathrm{ZPE}}{\mathrm{d}V} = k_0$ — then $\Delta P = -k_0$ remains constant. This accounts for the nearly invariant differences between P_0 and P_1, P_2 at varying volumes, as shown in Fig. 4(c).

We next examine the influence of ZPE on the critical pressure of phase transition. The enthalpy of each phase is given by $H = (E_0 + \mathrm{ZPE}) + PV$. Phase transition occurs when the enthalpies of two competing phases equal. The pressure at which this condition is met defines the critical pressure P_{c} (see

supplementary materials):

$$P_c = -\frac{\Delta E_0}{\Delta V} - \frac{\Delta \mathrm{ZPE}}{\Delta V} = P_{c0} + \Delta P_c. \tag{7}$$

Thus, the pressure correction $\Delta P_c = -\frac{\Delta \mathrm{ZPE}}{\Delta V}$ induced by ZPE primarily originates from the differences in ZPE and volume at the transition point. As the ZPE difference increases and volume difference decreases, significant enhancement in the pressure correction ΔP_c due to NQEs can be expected. In the vicinity of B-to-Y transition under high pressures, the enthalpy data in Fig. 4(d) show that $P_{c0} \cong 61.44$ GPa, $P_c \cong 61.81$ GPa, and $\Delta P_c = 0.37$ GPa. From Table 1, the volume changes by $\Delta V \cong -4.41$ Å^3/f.u. and the ZPE changes by $\Delta \mathrm{ZPE} \cong 0.01$ eV/f.u., which give the critical pressure $\Delta P_c = -\frac{\Delta \mathrm{ZPE}}{\Delta V} \cong 0.36$ GPa. The agreement is excellent.

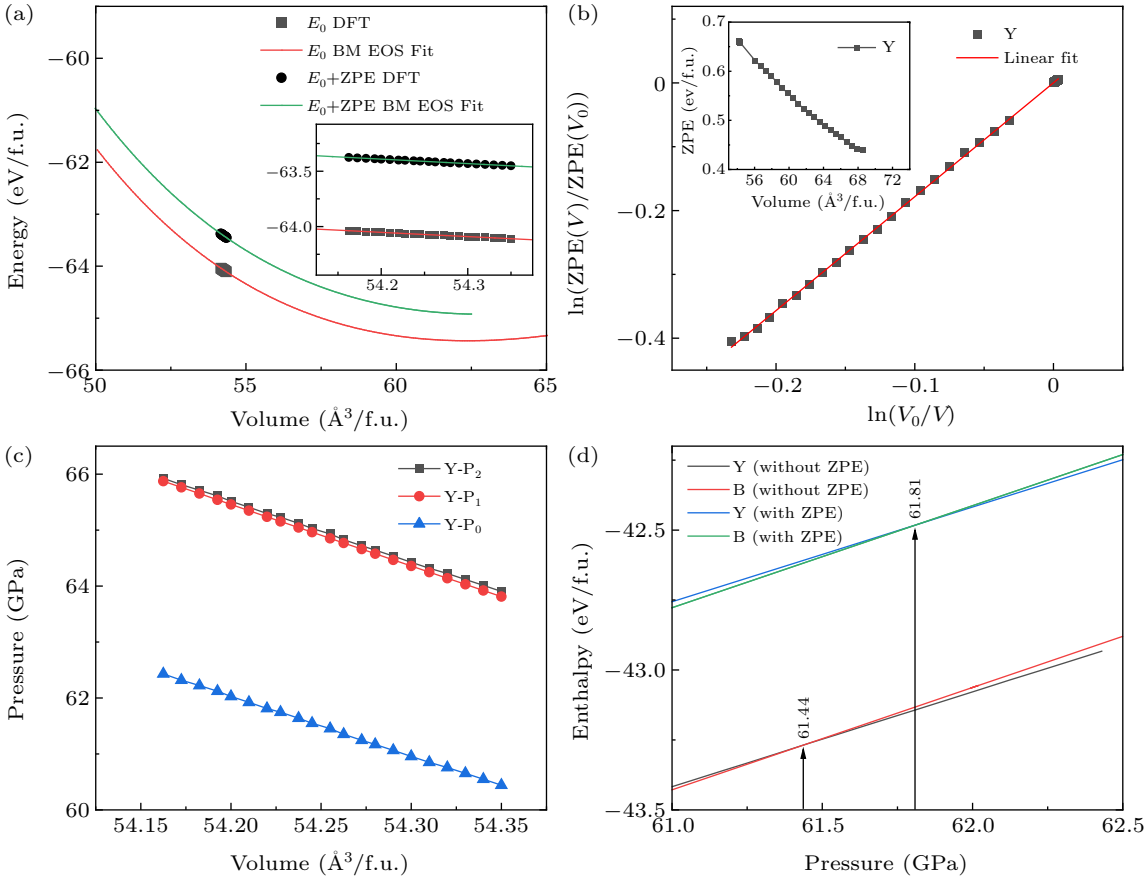


Fig. 4. (a) Total energy versus volume for Y-Ta_2O_5 near the phase transition point. The discrete points represent data calculated using DFT at different volumes. These data were fitted according to the third-order Birch–Murnaghan equation of state. (b) The dependence of ZPE with volume. (c) External pressure and its ZPE correction as functions of volume, where the subscripts 1 and 2 denote the data derived using the first and second schemes, respectively. (d) Enthalpies of the Y and B phases as a function of pressure, with the critical pressure point indicated, shown with and without ZPE correction.

To summarize, we predicted a high-pressure phase of Ta_2O_5 (Y-Ta_2O_5) with four formula units per crystal unit cell ($Z = 4$) using first-principles calculations combined with structural search algorithms. Our calculations show that B-Ta_2O_5 undergoes a transition to this new high-pressure polymorph at ~ 62 GPa, and Y-Ta_2O_5 remains as thermodynamically the most stable phase up to at least 200 GPa. Electronic structure calculations reveal that Y-Ta_2O_5 exhibits direct bandgap semiconducting behavior. We have further investigated the mutual relationship between external pressure and phonon vibrations. Near the critical phase transition pressure, our calculations demonstrate that zero-point energy (ZPE) corrections to the pressure values are non-negligible. This finding provides clear evidence that observable nuclear quantum effects (NQEs) exist even in non-light-element systems like transition metal oxides under high-pressure conditions.

Acknowledgments

Project supported by the National Natural Science Foundation of China (Grant Nos. 12074382, 11474285, and 12464012). We would like to thank Professor E. G. Wang for reading and helpful comments on the manuscript. We are grateful to the staff of the Hefei Branch of Supercomputing Center of Chinese Academy of Sciences, and the Hefei Advanced Computing Center for support of supercomputing facilities. We also thank the crew of the Center for Computational Materials Science, Institute for Materials Research of Tohoku University, and the supercomputer resources through the HPCI System Research Project (hp200246).

References

[1] Chu A K, Lu Y Y and Lin Y Y 2019 *Opt. Express* **27** 6629
[2] Lamee K F, Carlson D R, Newman Z L, Yu S P and Papp S B 2020 *Opt. Lett.* **45** 4192
[3] Zhang Z, Liu R, Wang W, Yan K, Yang Z, Song M, Wu D, Xu P, Wang X and Wang R 2023 *Opt. Lett.* **48** 5799
[4] Song S G, Cai S J, Han D X, García Nuñez C, Zhang G, Wallace G, Fleming L, Craig K, Reid S, Martin I W, Rowan S and Gibson D 2023 *Appl. Opt.* **62** B73
[5] Liu L F, Pan L Y, Zhang Z G and Xu J 2015 *Chin. Phys. Lett.* **32** 088501
[6] Sun S, Gao L, Han P, Zhu L, Li W M and Li A D 2024 *J. Mater. Chem. C* **12** 18676
[7] Wedig A, Luebben M, Cho D Y, Moors M, Skaja K, Rana V, Hasegawa T, Adepalli K K, Yildiz B, Waser R and Valov I 2016 *Nat. Nanotechnol.* **11** 67
[8] Kingon A I, Maria J P and Streiffer S K 2000 *Nature* **406** 1032
[9] Waser R, Dittmann R, Staikov G and Szot K 2009 *Adv. Mater.* **21** 2632
[10] Huerta-Flores A M, Ruiz-Zepeda F, Eyovge C, Winczewski J P, Vandichel M, Gaberscek M, Boscher N D, Gardeniers H, Torres-Martinez L M and Susarrey-Arce A 2022 *ACS Appl. Mater. Interfaces* **14** 31767
[11] Li R Y, Zhang Q Q, Li X S, Li N N, Liu X H and Li Z J 2025 *J. Electroanal. Chem.* **990** 119163
[12] Osuagwu B, Raza W, Tesler A B and Schmuki P 2021 *Nanoscale* **13** 12750
[13] Narangari P R, Karuturi S K, Wu Y, Wong-Leung J, Vora K, Lysevych M, Wan Y, Tan H H, Jagadish C and Mokkapati S 2019 *Nanoscale* **11** 7497
[14] Polydorou E, Verouti M, Soultati A, Armadorou K K, Verykios A, Filippatos P P, Galanis G, Tourlouki K, Kehayias N, Karatasios I, Kuganathan N, Chroneos A, Kilikoglou V, Palilis L C, Argitis P, Davazoglou D, Fakharuddin A, Mohd Yusoff A R b and Vasilopoulou M 2022 *Org. Electron.* **108** 106607
[15] Wang C, Zhou C H, Wang J G, Cho Y S, Wu W Y, Wuu D S, Huang C J and Lien S Y 2025 *Ceram. Int.* **51** 28791
[16] Singh E R, Almulhem N K, Alam M W and Singh N K 2024 *Opt. Mater.* **155** 115858
[17] Le Y, Ma X C, Xiao H D, Luan C N, Zhang B and Ma J 2023 *Appl. Phys. Lett.* **122** 252103
[18] Hosseini M, Khalil-Allafi J, Safavi M S and Ghalandarzadeh A 2025 *J. Alloys Compd.* **1023** 180193
[19] Hosseini M, Khalil-Allafi J and Safavi M S 2024 *J. Mater. Res. Technol.* **33** 4055
[20] Rafieerad A, Yan W, Alagarsamy K N, Srivastava A, Sareen N, Arora R C and Dhingra S 2021 *Adv. Funct. Mater.* **31** 2106786
[21] Lawson T, Joenathan A, Patwa A, Snyder B D and Grinstaff M W 2021 *ACS Nano* **15** 19175
[22] Bratash O, Courson R, Malaquin L, Leichle T, Buhot A, Leroy L and Engel E 2025 *Adv. Mater. Interfaces* **12** 2400941
[23] Rahman S, Azharuddin M and Tabassum R 2024 *Mater. Sci. Semicond. Process.* **178** 108457
[24] Pérez-Walton S, Valencia-Balvín C, Padilha A C M, Dalpian G M and Osorio-Guillén J M 2016 *J. Phys.: Condens. Matter* **28** 035801
[25] Terao N 1967 *Jpn. J. Appl. Phys.* **6** 21
[26] Zibrov I P, Filonenko V P, Sundberg M and Werner P E 2000 *Acta Crystallogr. B* **56** 659
[27] Tang H M and Yang Y 2024 *Chin. J. Phys.* **89** 1678
[28] Stephenson N C and Roth R S 1971 *Acta Crystallogr. Sect. B* **27** 1037
[29] Grey I E, Mumme W G and Roth R S 2005 *J. Solid State Chem.* **178** 3308
[30] Hummel H U, Fackler R and Remmert P 2006 *Chem. Ber.* **125** 551
[31] Fukumoto A and Miwa K 1997 *Phys. Rev. B* **55** 11155
[32] Aleshina L A and Loginova S V 2002 *Crystallogr. Rep.* **47** 415
[33] Ramprasad R 2003 *J. Appl. Phys.* **94** 5609
[34] Lee S H, Kim J, Kim S J, Kim S and Park G S 2013 *Phys. Rev. Lett.* **110** 235502
[35] Yang Y and Kawazoe Y 2018 *Phys. Rev. Mater.* **2** 034602
[36] Tong Y W, Tang H M and Yang Y 2023 *Comp. Mater. Sci.* **230** 112482
[37] Zheng B, Chen T, Sun H, Yang M, Yang B, Chen X, Zhang Y and Liu X 2024 *Chin. Phys. Lett.* **41** 057301
[38] Wang Y Q, Zhang C Z, Zhang J Q, Li S, Ju M, Sun W G, Dou X L and Jin Y Y 2023 *Chin. Phys. B* **32** 97402
[39] Qin T, Wu M, Wang K, Wu Y and Huang H 2024 *Chin. Phys. B* **33** 118101
[40] Zibrov I P, Filonenko V P, Sundberg M and Werner P E 2000 *Acta Crystallogr. Sect. B* **56** 659
[41] Markland T E and Ceriotti M 2018 *Nat. Rev. Chem.* **2** 0109
[42] Morales M A, McMahon J M, Pierleoni C and Ceperley D M 2013 *Phys. Rev. Lett.* **110** 065702
[43] Litman Y, Donadio D, Ceriotti M and Rossi M 2018 *J. Chem. Phys.* **148** 102320
[44] McKenzie R H, Bekker C, Athokpam B and Ramesh S G 2014 *J. Chem. Phys.* **140** 174508
[45] Andreani C, Colognesi D, Pietropaolo A and Senesi R 2011 *Chem. Phys. Lett.* **518** 1
[46] Senesi R, Flammini D, Kolesnikov A I, Murray E D, Galli G and Andreani C 2013 *J. Chem. Phys.* **139** 074504
[47] Meng X Z, Guo J, Peng J B, Chen J, Wang Z C, Shi J R, Li X Z, Wang E G and Jiang Y 2015 *Nat. Phys.* **11** 235
[48] Guo J, Lü J T, Feng Y X, Chen J, Peng J B, Lin Z, Meng X Z, Wang Z C, Li X Z, Wang E G and Jiang Y 2016 *Science* **352** 321
[49] Guo J, Li X, Peng J, Wang E G and Jiang Y 2017 *Prog. Surf. Sci.* **92** 203
[50] Wang E G 2024 *Full Quantum Effects in Condensed Matter Physics* (Beijing: Science Press)
[51] Yang Y and Kawazoe Y 2019 *J. Phys. Chem. C* **123** 13804
[52] Bi C and Yang Y 2021 *J. Phys. Chem. C* **125** 464
[53] Tong Y W and Yang Y 2024 *Chin. Phys. Lett.* **41** 086801
[54] Bi C, Chen Q, Li W and Yang Y 2021 *Chin. Phys. B* **30** 046601
[55] Tong Y W and Yang Y 2024 *J. Phys. Chem. C* **128** 840
[56] Lu B B, Kang D D, Wang D, Gao T Y and Dai J Y 2019 *Chin. Phys. Lett.* **36** 103102
[57] Kresse G and Hafner J 1993 *Phys. Rev. B* **47** 558
[58] Kresse G and Furthmüller J 1996 *Phys. Rev. B* **54** 11169
[59] Oganov A R and Glass C W 2006 *J. Phys. Chem. C* **124** 244704
[60] Zhu Q, Li L, Oganov A R and Allen P B 2013 *Phys. Rev. B* **87** 195317
[61] Wang Y C, Lv J, Zhu L and Ma Y M 2010 *Phys. Rev. B* **82** 094116
[62] Wang Y C, Lv J, Zhu L and Ma Y M 2012 *Comput. Phys. Commun.* **183** 2063
[63] Zhang X, Wang Y, Lv J, Zhu C, Li Q, Zhang M, Li Q and Ma Y 2013 *J. Chem. Phys.* **138** 114101
[64] Xu Z Z, Li J F, Geng Y L, Zhang Z B, Lv Y, Zhang C, Wang Q L and Wang X L 2023 *Chin. Phys. Lett.* **40** 076201
[65] Qu N R, Wang H C, Li Q, Li Z P and Gao F M 2019 *Chin. Phys. Lett.* **36** 036201
[66] Perdew J P, Burke K and Ernzerhof M 1996 *Phys. Rev. Lett.* **77** 3865
[67] Hedin L 1965 *Phys. Rev.* **139** A796
[68] Hybertsen M S and Louie S G 1986 *Phys. Rev. B* **34** 5390
[69] Baroni S, De Gironcoli S, Dal Corso A and Giannozzi P 2001 *Rev. Mod. Phys.* **73** 515
[70] Parlinski K, Li Z Q and Kawazoe Y 1997 *Phys. Rev. Lett.* **78** 4063
[71] Yang Y, Meng S and Wang E G 2006 *J. Phys.: Condens. Matter* **18** 10165
[72] Born M and Huang K 1954 *Dynamical Theory Of Crystal Lattices* (London: Oxford University Press)
[73] Huang K and Han R Q 1988 *Solid State Physics* (Beijing: Higher Education Press)
[74] Birch F 1947 *Phys. Rev.* **71** 809
[75] Murnaghan F D 1944 *Proc. Natl. Acad. Sci. USA* **30** 244
[76] Wang V, Xu N, Liu J C, Tang G and Geng W T 2021 *Comput. Phys. Commun.* **267** 108033
[77] Murnaghan F D 1937 *Am. J. Math.* **59** 235
[78] Katsura T and Tange Y 2019 *Minerals* **9** 745